pp. 1–15 (2018)

Numerical simulation of aberrated medical ultrasound signals

K. A. Beklemysheva[*], G. K. Grigoriev[†], N. S. Kulberg[‡], I. B. Petrov[*], A. V. Vasyukov[*§], and Yu. V. Vassilevski[§*¶]

Abstract — Transcranial ultrasound examination is hampered by the skull which acts as an irregular aberrator of the ultrasound signal. Numerical recovery of the ultrasound field can help in elimination of aberrations induced by the skull. In this paper, we address the simulation of medical phantom scanning through silicon aberrators with wave notching. The numerical model is based on the 2D acoustic equations which are solved by the wavefront construction raytracing method. Numerical B-scan images are compared with experimental B-scan images.

Keywords: medical ultrasound, raytracing, wavefront construction raytracing, model verification

MSC 2010: 65M25, 74J20

Direct and fast simulation of transcranial ultrasound investigations is the cornerstone of a prospective technology allowing to eliminate aberrations induced by the skull. These aberrations are the main barrier for the wide use of the transcranial ultrasound, a cheap and reliable mode for non-invasive investigation of intracranial tissues.

Another difficulty for simulation of the transcranial ultrasound is related to shear and surface waves [1,11,17]. The majority of models for medical ultrasound use the acoustic material model [26] that ignores shear and surface waves. This assumption works well for soft tissues and MHz frequencies that are used in the diagnostic ultrasound [19]. In fact, shear waves leave their trace on the signal generated by a region adjacent to the sensor and increase the blind area of the device, but they decay too quickly to reach anything else. However, longitudinal waves that fall on the contact between elastic bodies, generate shear waves and *vice versa* [1]. In bones, shear waves decay much slower and travel much faster than in soft tissues. In case

[*]MIPT, 9 Institutskiy per., Dolgoprudny, Moscow Region 141700

[†]MGTS Medical and health center, 12, bld. 1, Petrovsky Blvd., Moscow 127051

[‡]Moscow Scientific and Practical Center of Medical Radiology, 28, bld. 1, Srednaya Kalitnikovskaya Str, Moscow 109029; IEI FRC CSC RAS, 44, block 2, Vavilov Str, Moscow 119333

[§]INM RAS, 8 Gubkina Str, Moscow 119333

[¶]Sechenov University, 2/4, Bolshaya Pirogovskaya Str, Moscow 119991. E-mail: yuri.vassilevski@gmail.com

The research was supported by Russian Science Foundation grant 14-31-00024.

of the transcranial ultrasound, the shear and surface waves can produce a noise: they propagate around the skull and generate a longitudinal wave which leaves a signal on the sensor before the ultrasound response from blood vessels reaches it.

In principle, the numerical solution of the elastic equations accounts all these waves without delving into the physics of their generation. When a complete system of the elastic equations is solved at each grid node (including interfaces and contacts), these waves are taken into account automatically. One of the most relevant numerical methods for these purposes is the grid-characteristic method (GCM) [20]. It can manage any kind of boundary and contact conditions, it provides analysis of complex stress patterns with high spatial resolution [5, 6]. A reduced model represented by the acoustic equations can be successfully applied to the transcranial ultrasound simulation by the GCM [4]. However, in case of the transcranial ultrasound, the required spatial resolution leads to an unacceptable computing time. Another disadvantage of the GCM applied to the transcranial ultrasound simulation is that GCM merges wavefronts of the signal propagating in a complex multilayered medium. Waves merging complicates the analysis of the wave pattern. This analysis is essential for our final goal, elimination of aberrations induced by the skull. In this paper we restrict such analysis to a validation task, scanning of a medical phantom through a silicon aberrator.

An efficient numerical method which simplifies the analysis of interfering wave patterns at the cost of direct simulation of all wave processes, is the raytracing method [25]. It is used in many fields: computer graphics [30], radiolocation, underwater acoustic location, medical and industrial ultrasound, optics and seismics [8, 15], although we are not aware of surface waves simulation by the raytracing method. We applied successfully the raytracing method to simulation of diagnostic ultrasound and validation of the model on a phantom [28]: numerical B-scans coincide with B-scans produced by an ultrasonic scanner. For development of the raytracing methods we refer to [7, 9, 22, 23, 27].

The wavefront construction method (WCM) [13, 14, 18, 29] develops the conventional raytracing method further: instead of individual independent rays, wave fronts are modelled by front grids [15]. In 3D simulation the front is represented by a surface whose resolution can be dynamically varied by addition of new rays. Thus one avoids artificial shadows generated by the original method in the case of insufficient number of rays, and simulates point reflectors, objects that are too small to be accounted by the original method but are important for validation of the model on a phantom. The wavefront oriented method [10] increases the front resolution. It changes the way of the mesh refinement: instead of interpolating the neighbouring nodes, it recalculates the new ray node from the sensor. For a comparison of different methods we refer to [16].

In this paper, we develop further the WCM and apply it to the 2D acoustic material model. We propose two innovations: processing of propagation through interfaces between different materials according to the Snell's law and addition of point reflectors to the media. The method refines dynamically the wavefront mesh inserting new nodes to the mesh by interpolation of neighbouring nodes. It can process

point reflectors and intricate contact surfaces accounting reflection, refraction, and attenuation. The WCM allows us to simulate numerically the scanning of a medical phantom through a silicon aberrator with wave notching.

The paper is organized as follows. In Section 1 we present governing equations for the acoustic wave propagation and the WCM method. Section 2 provides analysis of wave patterns after passing through silicon aberrators and comparison of numerical and experimental B-scan images. Conclusive remarks are presented in Section 3.

1. Wavefront propagation in multi-material media

According to the acoustic model [21], the ultrasound signal propagation is described by the following equations:

$$\begin{aligned} \rho(\mathbf{x})\frac{\partial \mathbf{v}(\mathbf{x},t)}{\partial t} + \nabla p(\mathbf{x},t) = 0 \quad &\text{in } \Omega \\ \frac{\partial p(\mathbf{x},t)}{\partial t} + \rho(\mathbf{x})c^2(\mathbf{x})\nabla\cdot\mathbf{v}(\mathbf{x},t) = -\alpha(\mathbf{x})c(\mathbf{x})p(\mathbf{x},t) \quad &\text{in } \Omega \end{aligned} \tag{1.1}$$

where Ω is the domain occupied by biological tissues, $\mathbf{x}$ is a point in Ω, $\rho(\mathbf{x})$ is the tissue density, $\mathbf{v}(\mathbf{x},t)$ is the velocity vector, $p(\mathbf{x},t)$ is the acoustic pressure, $c(\mathbf{x})$ is the speed of sound, $\alpha(\mathbf{x})$ is the Maxwell's attenuation coefficient [4].

The acoustic model takes into account longitudinal (pressure) waves in soft tissues and does not account transverse (shear) waves. This model is conventional in diagnostic ultrasound simulations since the attenuation coefficient for shear waves in soft tissues is four orders of magnitude greater than that for pressure waves at MHz frequencies [19]. The skull bone does not damp the shear and surface waves, and the correct simulation of the transcranial ultrasound should involve both elastic material model and acoustic material model, including the processes at the contacts between elastic and acoustic materials. In this paper, we restrict ourselves by the acoustic model of the transcranial ultrasound leaving the multiphysics model to a future research. The reason for such simplification is that ultrasound propagation in a medical phantom with a silicon aberrator generates shear and surface waves which do not affect essentially the sonic field.

The direct application of the raytracing method [25] to the numerical solution of (1.1) is complicated by artificial shadows typical in medical problems. An aberrator (e.g., skull) with a complex shape distorts the wavefront increasing angle and distance between adjacent rays. In the basic raytracing method, the rays are calculated independently and we do not have means to correct and trace the rays divergence. In case of simple geometry (for example, several thick and wide layers or a single cylinder in a homogeneous medium), the amount of rays can be estimated *a priori*. Computational meshes for tissues of the human body are too intricate for the *a priori* estimate. Even medical phantoms have objects that are hard to resolve by the conventional raytracing. Indeed, point reflectors within phantoms are usually implemented as thin (0.1 mm) nylon threads suspended in a phantom filler whose

characteristic size is 10-20 cm. The straightforward application of the raytracing method requires a prohibitively large number of rays in this case.

The wavefront construction method (WCM) is free of the above deficiencies [13, 14, 18, 29] since it adapts raytracing locally and dynamically. In 3D simulations, wavefronts are surfaces that can be approximated by triangular grids whose advancing is an issue [15]. In 2D simulations, wavefronts become curves that can be approximated by polylines and their advancing can be implemented relatively easy. In this paper, we reconstruct the ultrasonic field in a medical phantom with a notching aberrator where objects outside the focused ultrasound ray do not affect the signal on the sensor and the 2D model is sufficient.

We improve the WCM in two ways. The first innovation is the use of the Snell's law [1] for ray propagation at interfaces between different materials. We found that the wavefront reconstruction after its reflection and refraction has a lot of technical complexities and the Snell's law gives a key to the correct reconstruction. The second contribution is the account of point reflectors: when a wavefront segment crosses a point reflector, it emits a reflected spherical wave.

In the 2D case a wavefront in a medium is represented as a chain of interconnected nodes where wave intensity or amplitude is collocated. In our case the intensity corresponds to the acoustic pressure. Each node defines the current position of a ray. Propagation of these rays causes the wavefront advancing.

Propagation of a ray at each time step is calculated as follows:

$$\mathbf{d} = \mathbf{v}c\tau \tag{1.2}$$

where $\mathbf{d}$ is the displacement of the node representing the ray, $\mathbf{v}$ is the unit vector that defines the ray direction, c is the speed of sound in the medium, τ is the current time step. During the ray propagation, Maxwell's attenuation damps the wave intensity and after each time step the new ray intensity $\hat{p}$ is a portion of the current intensity $\bar{p}$:

$$\hat{p} = \bar{p}(1 - \alpha\tau) \tag{1.3}$$

where α denotes the effective attenuation coefficient of the medium. Formulae (1.2)–(1.3) provide the first order accuracy for time integration that is sufficient for our purposes.

The wavefront propagation in a homogeneous medium without obstacles is performed by simple Algorithm 1.1. The last step of Algorithm 1.1 provides the refinement of the wavefront, if necessary. Since the wavefront may participate in multiple interactions with contacts between materials and point reflectors, it is desired to have its ray field dense enough. The last step provides such density.

Algorithm 1.1 is not applicable when the wavefront approaches a contact interface between two materials (see Fig.1). The acoustic ray A reaching the interface, generates two rays, the reflected ray B (heading back to the same material) and the refracted ray C (heading towards the second material).

The directions of rays B and C are calculated according to the Snell's law [1]:

$$\sin(i_B)/c_B = \sin(i_C)/c_C = q \tag{1.4}$$

Algorithm 1.1 Ray propagation in a homogeneous medium.

```
1:  while simulation time limit is not reached do
2:    for all rays do
3:      move the ray node according to its displacement d (1.2)
4:      calculate the new ray intensity p̂ using (1.3)
5:    end for
6:    for all segments between rays do
7:      if segment length exceeds a threshold then
8:        insert the new ray node in the middle of the segment
9:      end if
10:   end for
11: end while
```

where i_B (i_C) is the angle between the surface normal vector and the direction $\mathbf{v}_B$ ($\mathbf{v}_C$), c_B and c_C are speeds of sound in the corresponding media, q is the wave parameter which remains constant for each reflection. The ray intensities p_B and p_C are calculated according to the following formula [1]:

$$\frac{p_B}{p_A} = -\frac{\rho_B \cos(i_C)/c_C - \rho_C \cos(i_B)/c_B}{\rho_B \cos(i_C)/c_C + \rho_C \cos(i_B)/c_B)} \tag{1.5}$$

$$\frac{p_C}{p_A} = \frac{2\rho_C \cos(i_B)/c_B}{\rho_B \cos(i_C)/c_C + \rho_C \cos(i_B)/c_B} \tag{1.6}$$

where ρ_B (ρ_C) is the density of the medium B (C), p_A is the intensity of the incident ray A.

To avoid the wavefront bifurcation complicating the wave pattern analysis, we generate two wavefronts (reflected and refracted) at the contact instance. Each new wavefront will propagate on its own, will interact with contact interfaces and point reflectors, will have its own refinement logic, etc.

To handle the reflected and refracted wavefronts at the contact interfaces, we use the following algorithm with virtual neighbours:

Figure 1 illustrates the case when incident ray A has real neighbours. Black points designate current positions of the rays, solid segments designate real neighbours, and dashed segments designate virtual neighbours. The rays B and C have the same position as the ray A at the contact instance, they distinguish from ray A only for the sake of illustration.

The situation when the incident ray A has virtual neighbours is presented in Fig .2. This scheme represents the next time step – ray A was replaced with rays

Algorithm 1.2 Ray propagation through a contact interface.

```
1: for all rays do
2:   if incident ray A reaches a contact interface then
3:     create new nodes representing ray B and ray C (see Fig. 1)
4:     calculate directions and intensities of rays B and C using (1.4)–(1.6)
5:     for all neighbour nodes of ray A do
6:       if the neighbour is a real neighbour then
7:         the neighbour becomes virtual neighbour for rays B and C
8:       end if
9:       if the neighbour is a virtual neighbour then
10:        if the neighbour resides in the same material as ray B then
11:          the neighbour becomes real neighbour for ray B
12:        else if the neighbour resides in the same material as ray C then
13:          the neighbour becomes real neighbour for ray C
14:        end if
15:      end if
16:    end for
17:    delete ray A and proceed with rays B and C
18:  end if
19: end for
```

B and C, all nodes (rays) were moved. The new incident ray is designated as A', the new reflected and refracted rays as B' and C', respectively. Real neighbours of ray A' are handled as explained above: right real neighbour of ray A' becomes right virtual neighbour for rays B' and C'. Left virtual neighbours of ray A' (rays B and C actually) become real neighbours for rays B' and C', according to the material they belong to.

The point reflectors are taken into account by similar Algorithm 1.3. When the wavefront reaches a point reflector, the reflector generates an effective echo with the following amplitude of the reflected wave p_r:

$$p_r = p_i s \cdot \mathrm{e}^{-t^2/2\tau^2} \cdot \cos(\omega t) \tag{1.7}$$

where t is the time, p_i is the amplitude of the wavefront at the point where the reflector resides, parameter s is the reflection intensity coefficient for the reflector,

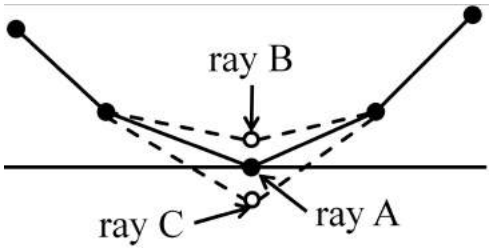

Figure 1. Wavefronts during simple reflection and refraction.

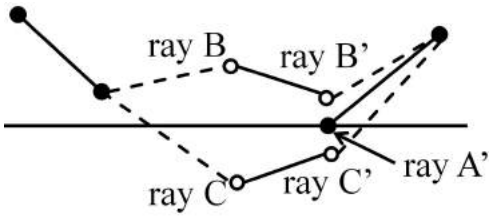

Figure 2. Reconstruction of wavefront after reflection and refraction.

parameter ω is the carrier frequency, parameter τ depends on the size of the transmitter and the speed of sound. The raytracing algorithm for point reflectors is as follows:

Algorithm 1.3 Ray reflection from a point reflector.

1: **for all** segments between rays **do**
2: **if** segment crosses a point reflector **then**
3: generate new rays representing the echo with parameters (1.7)
4: insert new rays into the segment
5: **end if**
6: **end for**

To illustrate the results of Algorithms 1.1 and 1.2, we consider the contact between two materials shown in Fig. 3 and a point transmitter of the ultrasound signal. Both materials are assumed to be homogeneous, and the intermediate (blue) layer may have different rheological properties. The reflected and refracted wavefronts vary for different speeds of sound in the intermediate layer and in the external material:

— the front of the head wave in the material with a lower speed of sound has the expected shape of a ‘bow’ (see [1]);

— the reflection is weaker when the material properties of the intermediate layer and the external medium are close;

— after passing through the obstacle, the shape of the wavefront is restored.

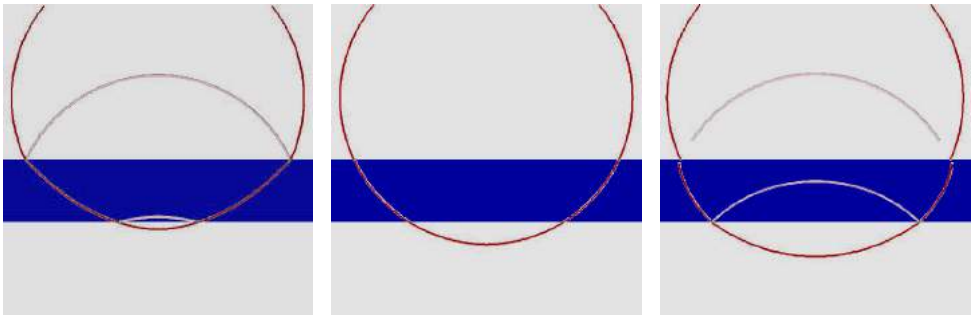

(a) (b) (c)

Figure 3. Wave pattern after passing the intermediate layer with different relative speed of sound: (a) 80% of the speed of sound in the external medium, (b) 100%, (c) 120%.

2. Numerical simulation of aberrated ultrasound signal

2.1. Characteristics of ultrasound signal, phantom and aberrator

Ultrasound scanner Medelkom 3.0S19 with a linear phased array of 64 elements was used for this research. Operational frequencies vary from 2 MHz to 7.5 MHz. The signal from each element has the following form:

$$p(\mathbf{x},t) = p_0 \int_{\omega_0-\Delta\omega}^{\omega_0+\Delta\omega} \mathrm{e}^{-\mathrm{i}(\omega t-\mathbf{kx})}\mathrm{d}\omega$$

where ω is the frequency, $\mathbf{k}$ is the wave vector, ω_0 is the transmitter base frequency, $\Delta\omega$ is determined by transmitter characteristics, p_0 is the amplitude independent of the frequency. The transmitted signal for our measurements has the base frequency ω = 3 MHz and $\Delta\omega$ = 1 MHz, and the meaningful part of the spectrum ranges from 0 to 6 MHz. Experimental data is digitized using 12 MHz frequency. The numerical model generates image samples with the same frequency so that the direct comparison between experimental and virtual images is possible. Each ray falling on an element leaves a single signal on it.

The ultrasound phantom ATL Labs, Model 539 Multipurpose Phantom [2] is used for validation of the numerical model. It contains multiple point reflectors with brightness 5%.

The aberrator is flat on one side and has a wavy surface on the other side. Two shapes of the aberrator are considered, with five waves and with three waves on the wavy (notched) surface. The casting mold was printed on a 3D printer, the general form of the mold for the five-wave aberrator is presented in Fig. 4.

Signal processing and B-scan image generation are discussed in [28]. The signal processing is based on the narrowband filtering and Hilbert transformation [3, 24] which eliminate the carrying frequency from the resulting signal.

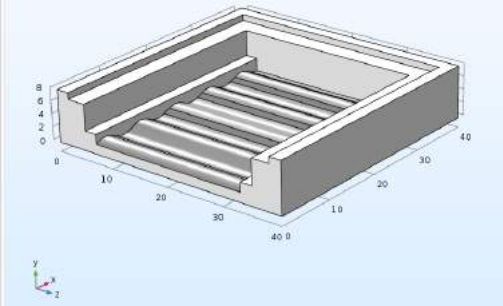

Figure 4. General view of the casting mold for the silicon aberrator with five waves.

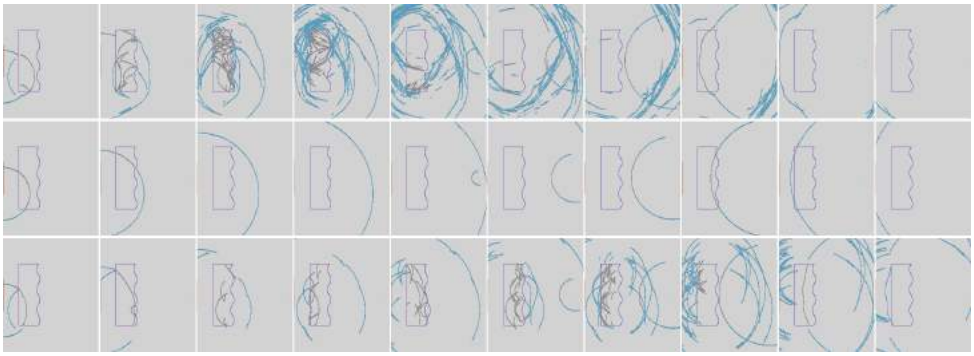

Figure 5. Propagation of a spherical wavefront through the three-wave notched aberrator and its reflection from a single point reflector. The notched side faces the phantom. From left to right: wave patterns at consequent time instances. From top to bottom: relative speed of sound in the aberrator is 70%, 100%, and 143%.

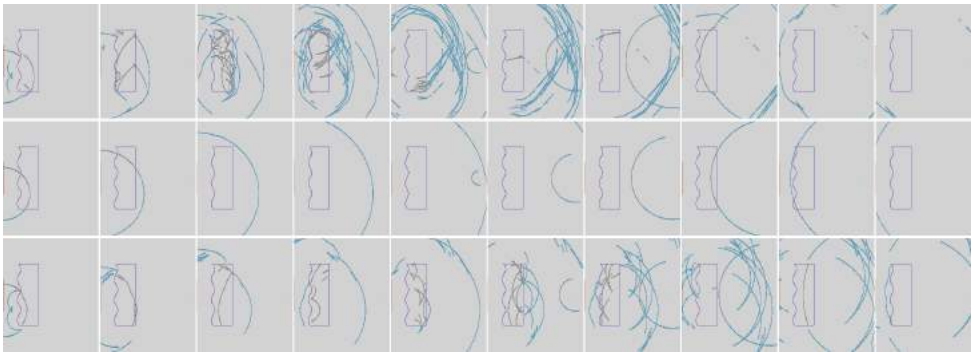

Figure 6. Propagation of a spherical wavefront through the three-wave notched aberrator and its reflection from a single point reflector. The notched side faces the sensor. From left to right: wave patterns at consequent time instances. From top to bottom: relative speed of sound in the aberrator is 70%, 100%, and 143%.

2.2. Analysis of virtual aberration and reflection

In order to analyze the influence of a wave-notched aberrator on propagation of a spherical wavefront and its reflection from a point reflector, we consider several virtual experiments.

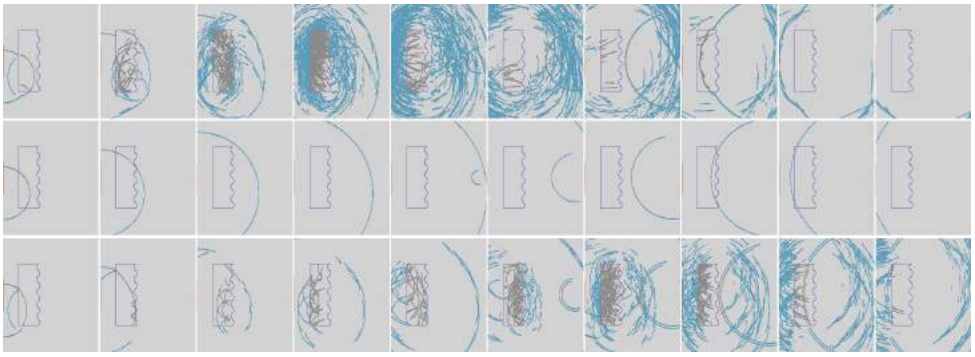

Figure 7. Propagation of a spherical wavefront through the five-wave notched aberrator and its reflection from a single point reflector. The notched side faces the phantom. From left to right: wave patterns at consequent time instances. From top to bottom: relative speed of sound in the aberrator is 70%, 100%, and 143%.

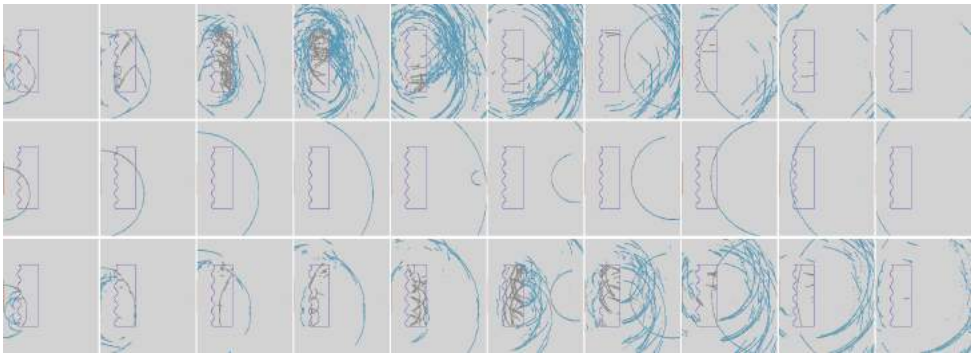

Figure 8. Propagation of a spherical wavefront through the five-wave notched aberrator and its reflection from a single point reflector. The notched side faces the sensor. From left to right: wave patterns at consequent time instances. From top to bottom: relative speed of sound in the aberrator is 70%, 100%, and 143%.

Figures 5 and 6 show the dynamic wave patterns for the three-wave notched aberrator and a single point reflector. The position of the reflector is chosen so that its signal reaches the sensor later than the reflected signal from the aberrator. Analogously, Figures 7 and 8 show the dynamic wave patterns for the five-wave notched aberrator. In each pair, the figures distinguish in the orientation of the notched side of the aberrator. We consider three virtual aberrator materials with the speed of sound equal to 70%, 100%, and 143% of that in the background material. Note that the second aberrator material provides no impact on the wave pattern.

Multiple reflections in the aberrator complicate the wave pattern dramatically. Each curve of the aberrator notching reflects a distinct wave. These waves overlap and produce more reflections each time when they reach the notched surface. In the numerical simulation by the grid characteristic method, these wavefronts merge into a wide weak wavefront. The raytracing method recovers every wavefront and allows us to backtrack all of them.

Since the initial pulse is strong, it generates several reflected waves, their exact

amount depends on the attenuation parameter and the relative speed of sound. The wave reflected from the point reflector is much weaker and its reflections from the aberrator are negligible.

The above analysis allows us to predict numerically the B-scan image of a spherical wavefront propagating through the aberrator. The focusing algorithm of the B-scan generation interprets the spherical wavefront as a point in the center of the sphere. If this point is not in the focusing direction or is too far from the focusing distance, it will be blurry. In the presence of the aberrator, each curve of its notched side gives a shadow of the point reflector. The closer the point reflector to the aberrator and sensor is, the smaller is the distance between these shadows.

Virtual B-scans (see Figs. 9 and 10) show that the point reflector signal can be easily lost in the reflections from the aberrator boundaries. Indeed, if the notched side of the aberrator faces the sensor, one can see distinct bright spots that are generated by reflections from the notches.

2.3. Propagation in aberrator and medical phantom: numerical vs. experimental data

The comparison of experimental and numerical B-scan images is given in Fig. 11. Without the aberrator, the numerical B-scan corresponds to the experimental image. Due to the signal processing algorithms, the size of point reflectors in the numerical B-scan is larger than in the experimental image.

On the experimental B-scan image, the three-wave aberrator multiplies the vertical group and the axial-lateral resolution group (a dense group of points near the center of the B-scan). On the numerical B-scan image, the vertical group of points is doubled similarly to the experimental image. The amplitude of the duplicate points is lower than that observed experimentally.

On the other hand, in the experimental image, the dead zone group is invisible without the aberrator, although is clearly visible in its presence, see the top of the image. In the numerical model, the dead zone group is also invisible without the aberrator. In its presence, the group points appear to be smeared out due to the signal processing algorithms.

3. Conclusions

In this article, we simulated the scanning of medical phantom through silicon aberrators with wave notching. The wavefront construction method for the 2D acoustic equations allowed us to reconstruct the reflected and refracted wave patterns using the virtual neighbours technique. The numerical B-scan images have shown good agreement with experimental B-scan images. Computational analysis of interaction of wavefronts with the aberrator explains the nature of aberrations observed on the experimental B-scan images.

Thus the WCM method is validated for the medical phantom. For application of the WCM to the transcranial ultrasound simulation, several modifications of the method must be made. First, one has to implement the elastic material model for

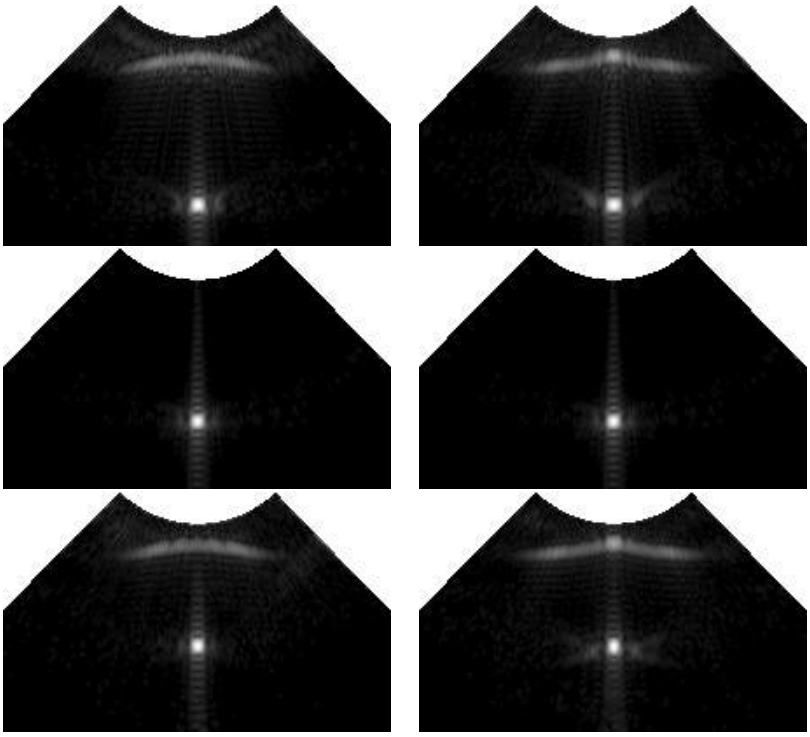

Figure 9. B-scans for the three-wave notched aberrator and the single point reflector. The notched side faces the phantom (left), the notched side faces the sensor (right). From top to bottom: relative speed of sound in the aberrator is 70%, 100%, and 143%.

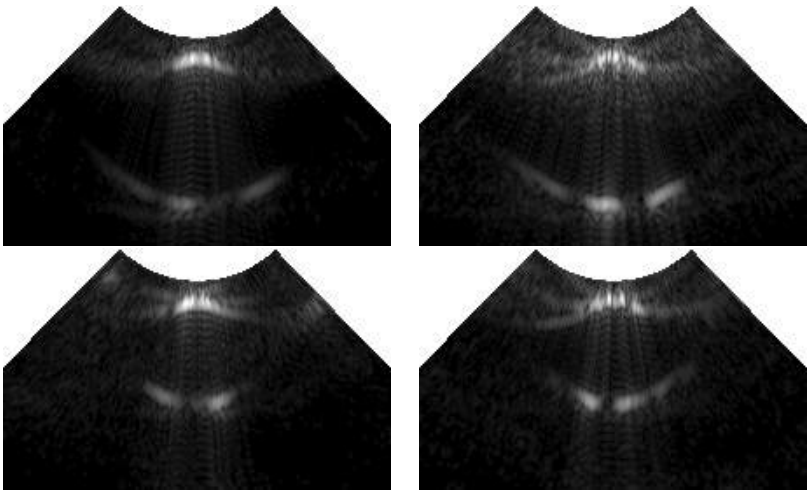

Figure 10. B-scans for the five-wave notched aberrator and the single point reflector. The notched side faces the phantom (left), the notched side faces the sensor (right). From top to bottom: relative speed of sound in the aberrator is 70%, 100%, and 143%.

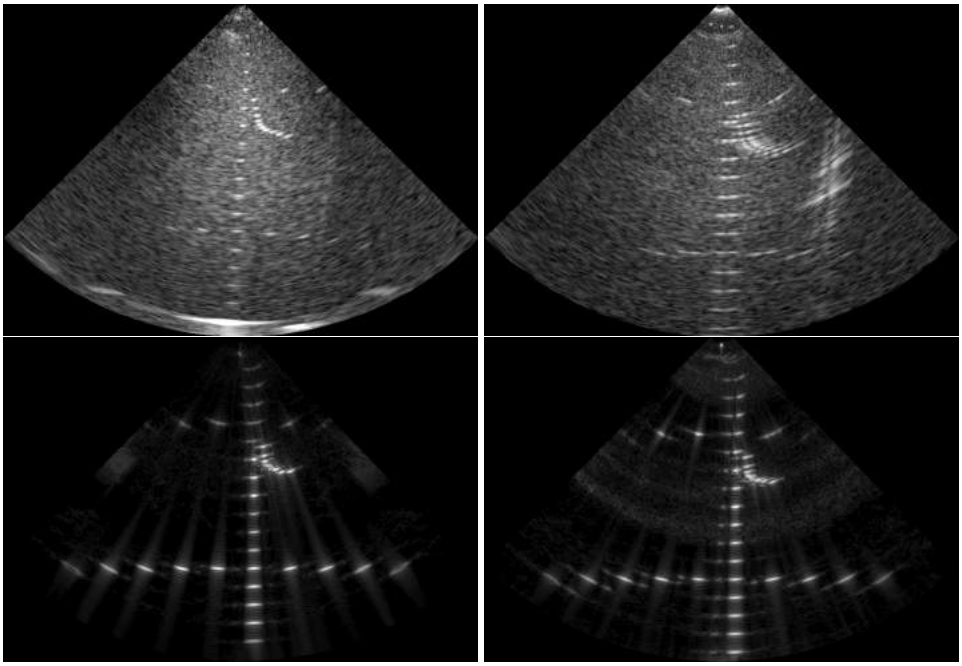

Figure 11. Comparison of experimental and numerical data: scanning without the aberrator (left), scanning through the three-wave notched aberrator (right). On the top row the experimental images are presented, on the bottom row the numerical images are shown.

the skull, incorporate the contact between elastic (bone) and acoustic (soft tissues) materials. Second, the human craniocerebral region requires the 3D simulation and therefore the 3D extension of the method.

The final goal of this long-term work is to develop a methodology for modelling of the transcranial ultrasound in domains close to real anatomy, and numerical elimination of aberrations induced by the skull.

References

1. K. Aki and P. Richards, *Quantitative Seismology. Theory and Methods.* W. H. Freeman and Company, San Francisco, 1980.
2. ATL Labs, Model 539 Multipurpose Phantom, http://www.atslaboratories-phantoms.com/resources/2012-539.pdf
3. S. I. Baskakov, *Radio Engineering Circuits and Signals: Textbook for High Schools*. Vysshaya Shkola, Moscow, 1988 (in Russian).
4. K. Beklemysheva, A. Danilov, G. Grigoriev, A. Kazakov, N. Kulberg, I. Petrov, V. Salamatova, A. Vasyukov, and Yu.Vassilevski, Transcranial ultrasound of cerebral vessels in silico: proof of concept. *Russ. J. Numer. Anal. Math. Modelling* **31** (2016), No. 5, 317–328.
5. K. Beklemysheva, A. Danilov, I. Petrov, V. Salamatova, Yu. Vassilevski, and A. Vasyukov, Virtual blunt injury of human thorax: age-dependent response of vascular system. *Russ. J. Numer. Anal. Math. Modelling* **30** (2015), No. 5, 259–268.

6. K. A. Beklemysheva, A. S. Ermakov, I. B. Petrov, and A. V. Vasyukov, Numerical simulation of the failure of composite materials by using the grid-characteristic method. *Math. Models Comput. Simul.* **5** (2016), No. 8, 557–567.
7. S. Buske and U. Kastner, Efficient and accurate computation of seismic traveltimes and amplitudes. *Geophys. Prosp.* **52** (2004), 313–322.
8. V. erven, *Seismic Ray Theory*. Cambridge University Press, New York, 2001.
9. V. erven, Seismic rays and ray intensities in inhomogeneous anisotropic media. *Geophys. J. R. Astr. Soc.* **29** (1972), 1–13.
10. R. Coman and D. Gajewski, Ray tracing by wavefront construction in 3-D, anisotropic media. *71st Internat. Meeting Abstract, Soc. Expl. Geophys.* (2001) 1265–1268.
11. S. Crampin, The dispersion of surface waves in multilayered anisotropic media. *Geophys. J. R. Astr. Soc.* **21** (1970), 387–402.
12. S. Kim and R. Cook, 3-d traveltime computation using second-order ENO scheme. *Geophysics* **64** (1999), 1867–1876.
13. H.-L. Lai, R. L. Gibson Jr., and K.-J. Lee, Quasi-shear wave raytracing by wavefront construction in 3-D anisotropic media. *J. Appl. Geophys.* **69** (2009), 82–95.
14. G. Lambare, P. S. Lucio, and A. Hanyga, Two-dimensional multivalued traveltime and amplitude maps by uniform sampling of a ray field. *Geophys. J. Int.* **125** (1996), 584–598.
15. K. J. Lee, Efficient ray tracing algorithms based on wavefront construction and model based interpolation method. *Doctoral Dissertation*. M. S., Texas A&M University, (2005).
16. A. Leidenfrost, N. Ettrich, D. Gajewski, and D. Kosloff, Comparison of six different methods for calculating traveltimes. *Geophys. Prosp.* **47** (1999), 269–297.
17. Lord Rayleigh, On waves propagated along the plane surface of an elastic solid. *Proc. London Math. Soc.* **1** (1885), 4–11.
18. P. S. Lucio, G. Lambare, and A. Hanyga, 3D multidimensional travel time and amplitude maps. *Pure Appl. Geophys.* **148** (1996), 449–479.
19. E. L. Madsen, H. J. Sathoff, and J. A. Zagzebski, Ultrasonic shear wave properties of soft tissues and tissue-like materials. *J. Acoust. Soc. Am.* **74** (1983), No. 5, 1346–1355.
20. K. M. Magomedov and A. S. Kholodov, The construction of difference schemes for hyperbolic equations based on characteristic relations. *USSR Comput. Math. Math. Physics* **2** (1969), No. 9, 158–176.
21. T. D. Mast, L. M. Hinkelman, L. A. Metlay, M. J. Orr, and R. C. Waag, Simulation of ultrasonic pulse propagation, distortion, and attenuation in the human chest wall. *J. Acoust. Soc. Amer.* **6** (1999), 3665–3677.
22. T. J. Moser, Shortest path calculation of seismic rays. *Geophysics* **56** (1991), 59–67.
23. J. Qian and W. Symes, An adaptive finite-difference method for traveltimes and amplitudes. *Geophysics* **67** (2002), 167–176.
24. A. B. Sergienko, *Digital Signal Processing*. St. Petersburg, 2006 (in Russian).
25. G. H. Spencer and M. V. R. K. Murty, General ray tracing procedure. *J. Opt. Soc. Amer.* **52** (1962), No. 6, 672–678.
26. N. M. Tole and H. Ostensen, *Basic Physics of Ultrasonographic Imaging*. World Health Organization, 2005.
27. H. J. A. van Avendonk, A. J. Harding, J. A. Orcutt, and W. S. Holbrook, Hybrid shortest path and ray bending method for traveltime and raypath calculation. *Geophysics* **66** (2001), 648–653.

28. Yu. Vassilevski, K. Beklemysheva, G. Grigoriev, N. Kulberg, I. Petrov, and A. Vasyukov, Numerical modelling of medical ultrasound: phantom-based verification. *Russ. J. Numer. Anal. Math. Modelling* **32** (2017), No. 5, 339–346.

29. V. Vinje, E. Iversen, and H. Gjystdal, Traveltime and amplitude estimation using wavefront construction. *Geophysics* **58** (1993), 1157–1166.

30. I. Wald, W. R. Mark, J. Gunther, S. Boulos, T. Ize, W. Hunt, S.G. Parker, and P. Shirley, State of the art in ray tracing animated scenes. In: *Eurographics 2007 State of the Art Reports*, 2007, 89–116.